



A novel peridynamics refinement method with dual-horizon peridynamics

Zhixin Zeng¹ · Xiong Zhang¹

Received: 3 January 2024 / Accepted: 9 April 2024

© The Author(s), under exclusive licence to Springer-Verlag London Ltd., part of Springer Nature 2024

Abstract

A novel adaptive refinement method is proposed for ordinary state-based PD in both 2D and 3D simulation. We perform an efficient adaptive refinement by splitting a parent particle into several child particles directly which does not require any information from its adjacent particles. The state variables and neighbor list of the child particles can be obtained directly from their parent particles, so that the proposed adaptive refinement method is very efficient and can be easily applied in both 2D and 3D cases without complex adjacent particle list building. To maintain simulation accuracy, the deformation of the parent particles need to be taken into consideration in the refinement process. Therefore, the accumulated strain of a PD particle is defined to calculate the position vector of its child particles in current configuration. With the consideration of the deformation of the parent particle, the fake damage is avoid. And a new criterion is established based on the particle accumulated strain to efficiently determine the particles need to be refined. The numerical examples studied show that the proposed adaptive refinement correctly captures the complicated crack propagation process and eliminates the fake crack growth with slight extra simulation cost, compared to the coarse discretization.

Keywords Peridynamics · Adaptive refinement · Dynamic fracture · Dual-horizon

1 Introduction

The prediction of the dynamic fracture initiation and propagation is an important issue in many engineering problems. Many efforts have been devoted to simulate the dynamic crack growth based on the finite element method (FEM), such as the cohesive zone method (CZM) [1] and the extended finite element method (XFEM) [2]. And many kinds of meshfree methods have been proposed aiming at modeling fracture problems, such as the augment Lagrangian element-free (ALEF) [3], the Element-Free Galerkin method (EFG) [4, 5], the cracking-particle method [6], material point method with crack (CRAMP) [7] and material point method with enriched shape function (EMPM) [8].

In recent years, peridynamics (PD) [9–11] has attracted widely interests in simulating crack problems. PD is based on non-local governing equations, and shows great flexibility in modeling dynamic fractures because the internal force relies on the interaction between particles. With the use of PD, the crack propagation happens naturally without explicitly tracking crack surface, and cracking initiation problem can be well simulated. There are three types of PD formulations: bond-based PD [10], ordinary state-based PD [12] and non-ordinary state-based PD [13, 14]. Silling [9–11] presented the bond-based PD as the bond acting like independent springs, and the internal force between two particles only related to their relative position. To overcome the restriction of Poisson's ratio in bond-based PD, two state-based PD formulations [12–14] have been proposed, in which the internal force between two particles depend not only on their relative position, but also on the deformation state of their horizon.

Because of the great flexibility in modeling dynamic fractures of PD, various works have been done based on these three PD formulations. Madenci et al. [15] presented a PD Least Squares Minimization (LSM) approach to construct explicit analytical expressions in integral form for PD approximation of a field variable and its derivatives. Silling

Supported by the National Natural Science Foundation of China (11672154).

✉ Xiong Zhang
xzhang@tsinghua.edu.cn

¹ School of Aerospace Engineering, Tsinghua University, Beijing 100084, People's Republic of China

et al. [16] introduced a PD Eulerian model equipped with a Mie-Grüneisen equation of state to model shockwaves and impact phenomena. Madenci et al. [17] presented the ordinary state-based PD constitutive relations for plastic deformation based on the Von Mises yield criteria with isotropic hardening. Madenci et al. [18] derived the bond-based PD equations of motion based on the Neo-Hookean model under the assumption of incompressibility for hyperelastic membrane deformation. Roy et al. [19] derived the weak form of bond-based PD equilibrium equation on Anand's model and Talamini-Mao Anand (TMA) model for polymers with slight compressibility. Rabczuk et al. [20] proposed a new penalty method to model the contact for compressive fractures and impose the penetration conditions. Kamensky et al. proposed a novel contact model considering the frictional contact. Zhang et al. [21] and Oterkus et al. [22] proposed a systematic pull-out simulation scheme in the formwork of two dimensional axisymmetric domain with PD considering the interface frictional contact.

In PD, if two pairwise particles have different horizon sizes, the ghost force and the spurious wave reflection will appear. And the variation of the horizon size is an important tool in many researches, such as boundary treatment and the adaptive refinement of particles. To overcome this shortage, Silling et al. [23] employed a modified equilibrium equation using a new quantity called the partial stress, however it impairs the simplicity of the traditional PD. Foster et al. [24] proposed a power-law-based PD kernel function to mitigate the spurious wave reflection problems during multiscale modeling. The widely used solution is the dual-horizon Peridynamics (DH-PD) [25, 26], which naturally includes varying horizon sizes and completely eliminates the ghost force.

Because the high nonlinearity of the cracking process, PD needs to have a fine discretization near the crack tip to obtain a precise result. And internal force of PD is calculated by the integral in the horizon, which leads to low simulation efficiency if the fine discretization is used in the whole simulation domain. Therefore, some researchers proposed several adaptive refinement methods to increase the resolution only in the region near the crack path. Bobaru et al. [27] developed a uniform refinement method in local regions to analyze 1-D elastic wave propagation problems and studied the convergence of the proposed refinement method. After that, Bobaru and Ha [28] developed a non-uniform 2D refinement method for Bond-based PD by using quadtree method. In their methods, the physical properties of the refined node needs to be determined by the interpolation of its adjacent particles and the so-called "hanging" particles needs to be treated specially. Dipasquale et al. [29] proposed a novel adaptive refinement method by simply inserting new nodes at the mid points of the lines connecting adjacent nodes of the same refinement level and gave a new trigger concept based on the damage

state of the material, coupled with the existing energy based trigger. However, in their methods, some of the particles are no longer at the center of their volume, which will compromise the accuracy of numerical spatial integration. Ren et al. [25] gave a simple adaptive refinement method by simply splitting the particles with quadtree method. However, they do not consider the deformation of the particles, which will lead to a loss of accuracy when calculating the position vector of the refined particles in current configuration. Gu et al. [30] applied the refinement method proposed by Dipasquale [29] on the voronoi-based PD.

In this study, we propose a novel adaptive refinement method for ordinary state-based PD in both 2D and 3D simulation. We perform the adaptive refinement by directly splitting parent particles with considering their deformation state. The accumulated strain of the parent PD particles is defined to calculate the position vector of their child particles in current configuration. And a new criterion for the activation of the refinement is established based on the particle accumulated strain to efficiently determine the refinement region. And the DH-PD is used to avoid the ghost force and the spurious wave reflection due to the variable horizon sizes in the refinement process.

The remainder of the paper is organized as follows. In Sect. 2, we briefly introduce the theory of state-based PD and dual-horizon PD. In Sect. 3, the new algorithms for the adaptive refinement are detailedly presented. Section 4 studies several numerical examples to validate the proposed method, and Sect. 5 draws concluding remarks.

2 Peridynamics

2.1 Fundamentals of ordinary state-based PD

As shown in Fig. 1(a), in ordinary state-based PD [12], a non-local method is used to calculate the internal force, so that the equation of motion of particle \mathbf{x}_k is given by

$$\begin{aligned} \rho(\mathbf{x}_k, t)\ddot{\mathbf{u}}(\mathbf{x}_k, t) = & \int_{H_k} (\mathbf{T}(\mathbf{x}_k, t) \langle \mathbf{x}_j - \mathbf{x}_k \rangle \\ & - \mathbf{T}(\mathbf{x}_j, t) \langle \mathbf{x}_k - \mathbf{x}_j \rangle) dV_{\mathbf{x}_j} \\ & + \rho(\mathbf{x}_k, t)\mathbf{b}(\mathbf{x}_k, t), \end{aligned} \quad (1)$$

where $\mathbf{u}(\mathbf{x}_k, t)$ and $H_k = \{\mathbf{x}_j | (\mathbf{x}_j - \mathbf{x}_k)^2 < \delta^2\}$ denote the displacement and horizon of \mathbf{x}_k respectively, δ is the horizon size, \mathbf{b} is the density of external body force. $\mathbf{T}(\mathbf{x}_k, t)$ and $\mathbf{T}(\mathbf{x}_j, t)$ are the force vector states between the particles \mathbf{x}_k and \mathbf{x}_j . As shown in Fig. 1b, with the force density vector $\mathbf{t}_{kj}(\mathbf{u}_j - \mathbf{u}_k, \mathbf{x}_j - \mathbf{x}_k, t) = \mathbf{T}(\mathbf{x}_k, t) \langle \mathbf{x}_j - \mathbf{x}_k \rangle$ and particle integration, the motion Eq. (1) of particle \mathbf{x}_k in the deformed configuration can be written as

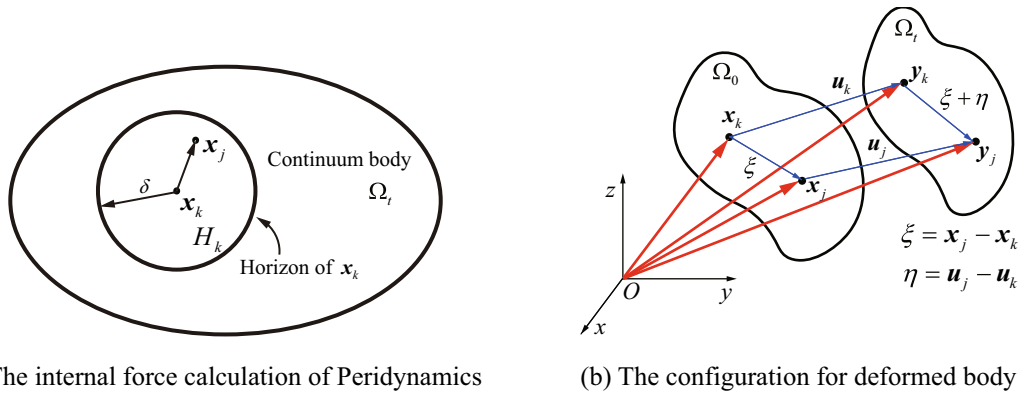


Fig. 1 Internal force calculation of Peridynamics

$$\begin{aligned}
 m(\mathbf{x}_k)\ddot{\mathbf{u}}(\mathbf{x}_k, t) = & \sum_{x_j \in H_k} [\mathbf{t}_{kj}(\mathbf{u}_j - \mathbf{u}_k, \mathbf{x}_j - \mathbf{x}_k, t) \\
 & - \mathbf{t}_{jk}(\mathbf{u}_k - \mathbf{u}_j, \mathbf{x}_k - \mathbf{x}_j, t)] V_j V_k \\
 & + m(\mathbf{x}_k)\mathbf{b}(\mathbf{x}_k, t).
 \end{aligned} \tag{2}$$

In ordinary state-based PD, the force density vector, $\mathbf{t}_{kj}(\mathbf{u}_j - \mathbf{u}_k, \mathbf{x}_j - \mathbf{x}_k, t)$, can be given by the strain energy density function as

$$\mathbf{t}_{kj}(\mathbf{u}_j - \mathbf{u}_k, \mathbf{x}_j - \mathbf{x}_k, t) = \frac{1}{V_j} \frac{\partial W_k}{\partial |\mathbf{y}_j - \mathbf{y}_k|} \frac{\mathbf{y}_j - \mathbf{y}_k}{|\mathbf{y}_j - \mathbf{y}_k|}, \tag{3}$$

where $\mathbf{y}_j = \mathbf{x}_j + \mathbf{u}_j$ and W_k is the strain energy density function of particle \mathbf{x}_k . For elastic material, the strain energy density function W_k can be written as

$$W_k = a\theta_k^2 + b\delta \sum_{x_j \in H_k} \frac{(|\mathbf{y}_j - \mathbf{y}_k| - |\mathbf{x}_j - \mathbf{x}_k|)^2}{|\mathbf{x}_j - \mathbf{x}_k|} V_j, \tag{4}$$

where

$$\begin{aligned}
 \theta_k &= d\delta \sum_{x_j \in H_k} \frac{(\mathbf{x}_j - \mathbf{x}_k) \cdot (\mathbf{y}_j - \mathbf{y}_k)}{|\mathbf{x}_j - \mathbf{x}_k| |\mathbf{y}_j - \mathbf{y}_k|} s_{kj}, \\
 s_{kj} &= \frac{|\mathbf{y}_j - \mathbf{y}_k| - |\mathbf{x}_j - \mathbf{x}_k|}{|\mathbf{x}_j - \mathbf{x}_k|}
 \end{aligned} \tag{5}$$

is the bond stretch of two particles, a , b and d are the material parameters which can be derived from the shear modulus μ and bulk modulus κ by

$$a = \begin{cases} \frac{1}{2}(\kappa - \frac{5}{3}\mu) & \text{for 3D cases} \\ \frac{1}{2}(\kappa - 2\mu) & \text{for 2D cases} \end{cases}, \tag{6}$$

$$b = \begin{cases} \frac{15\mu}{2\pi\delta^5} & \text{for 3D cases} \\ \frac{6\mu}{\pi\delta^4 h} & \text{for 2D cases} \end{cases}, \tag{7}$$

$$d = \begin{cases} \frac{9}{4\pi\delta^4} & \text{for 3D cases} \\ \frac{2}{\pi h\delta^3} & \text{for 2D cases} \end{cases}. \tag{8}$$

Considering the damage of the bond, the motion Eq. (2) can be rewritten as

$$\begin{aligned}
 m(\mathbf{x}_k)\ddot{\mathbf{u}}(\mathbf{x}_k, t) = & \sum_{x_j \in H_k} \mu_{kj}(\mathbf{t}_{kj}(\mathbf{u}_j - \mathbf{u}_k, \mathbf{x}_j - \mathbf{x}_k, t) \\
 & - \mathbf{t}_{jk}(\mathbf{u}_k - \mathbf{u}_j, \mathbf{x}_k - \mathbf{x}_j, t)) V_j V_k \\
 & + m(\mathbf{x}_k)\mathbf{b}(\mathbf{x}_k, t),
 \end{aligned} \tag{9}$$

where the history-dependent scalar valued function μ_{kj} is determined by

$$\mu_{kj} = \begin{cases} 1 & s_{kj} < s_c \quad \forall t' < t \\ 0 & \text{otherwise} \end{cases}, \tag{10}$$

s_c is the critical bond stretch determined from the the shear modulus μ , bulk modulus κ and the energy release rate G_c of the crack face by

$$s_c = \begin{cases} \sqrt{\frac{G_c}{(3\mu + (\frac{3}{4})^4(\kappa - \frac{5}{3}\mu))\delta}} & \text{for 3D cases} \\ \sqrt{\frac{G_c}{(\frac{6\mu}{\pi} + \frac{16}{9\pi^2}(\kappa - 2\mu))\delta}} & \text{for 2D cases} \end{cases}. \tag{11}$$

The local damage value of particle \mathbf{x}_k is defined as

$$\phi_k = 1 - \frac{\sum_{x_j \in H_k} \mu_{kj} V_j}{\sum_{x_j \in H_k} V_j}. \tag{12}$$

To reduce the PD surface effect, the energy-based surface effect correction proposed by Madenci et al. [31] is used in this work.

2.2 Dual-horizon peridynamics

In our peridynamics refinement method, the material body is discretized into particles with different sizes. If a constant horizon is used for different particle sizes, the number of the neighbor particles will dramatically increase, which will decrease the computational efficiency significantly. And if a variable horizon is used for different particle sizes, the spurious wave reflections will happen in traditional PD, because the traditional peridynamics formulation with single horizon is not easy to account for the interaction between two particles with different horizon sizes [23, 26]. Therefore, the dual-horizon peridynamics (DH-PD) [26] is used in our adaptive particle refinement method.

In the traditional ordinary state-based Peridynamics the horizon $H_k = \{x_j | (x_j - x_k)^2 < \delta^2\}$ for particle x_k is a domain centered at the particle position with a radius of δ . In DH-PD, particle x_k has a traditional horizon $H_k = \{x_j | (x_j - x_k)^2 < \delta_k^2\}$ and a dual horizon $H'_k = \{x_j | x_k \in H_j\}$. Because the horizon size δ_k of each particle x_k is not necessarily same in DH-PD, the traditional horizon H_k is not equal to the dual horizon H'_k . As shown in Fig. 2, for particle x_k , particles x_1 and x_2 belong to the horizon $H_k = \{x_j | (x_j - x_k)^2 < \delta_k^2\}$, while particles x_1 and x_3 belong to the dual horizon $H'_k = \{x_j | x_k \in H_j\}$.

In DH-PD, the internal force of particle x_k is divided into two parts, and the motion Eq. (2) can be rewritten as

$$m(x_k)\ddot{u}(x_k, t) = \sum_{x_j \in H_k} \mu_{kj} \mathbf{t}_{kj}(u_j - u_k, x_j - x_k, t) V_j V_k - \sum_{x_j \in H'_k} \mu_{jk} \mathbf{t}_{jk}(u_k - u_j, x_k - x_j, t) V_j V_k + m(x_k) \mathbf{b}(x_k, t) \tag{13}$$

The first part of the right-hand side $\sum_{x_j \in H_k} \mu_{kj} \mathbf{t}_{kj}(u_j - u_k, x_j - x_k, t) V_j V_k$ is the sum of the direct force due to bond s_{kj} , and the parameters in Eqs. (6)–(8) to calculate the internal force $\mathbf{t}_{kj}(u_j - u_k, x_j - x_k, t)$ should be determined by the material parameters and the horizon size of particle x_k . On the other hand, the second part of the right-hand side $-\sum_{x_j \in H'_k} \mu_{jk} \mathbf{t}_{jk}(u_k - u_j, x_k - x_j, t) V_j V_k$ is the sum of the reaction force due to bond s_{jk} , and the parameter in Eqs. (6)–(8) to calculate the internal force $\mathbf{t}_{jk}(u_k - u_j, x_k - x_j, t)$ should be determined by the material parameters and the horizon size of particle x_j . It is worth to mention that the history-dependent scalar valued function μ_{kj} and μ_{jk} may not be equal in DH-PD, because the critical stretch s_c of particle x_k and x_j are not necessarily equal due to the variation of the horizon size. Therefore, the bond s_{jk} and s_{kj} will break independently. The breakage of bond s_{kj} is determined by the critical stretch attached to the particle x_k , and breakage of bond s_{jk} is determined by the critical stretch attached to the particle x_j . As defined in Gu et al. [30], the damage value of particle x_k in Eq. (12) can be rewritten as

$$\phi_k = 1 - \frac{\sum_{x_j \in H_k} \mu_{kj} V_j + \sum_{x_j \in H'_k} \mu_{jk} V_j}{\sum_{x_j \in H_k} V_j + \sum_{x_j \in H'_k} V_j} \tag{14}$$

3 Adaptive particle refinement scheme for PD

Because the high nonlinearity of the cracking process, PD needs to have a fine discretization near the crack tip to obtain a precise result. And internal force of PD is calculated by the integral in the horizon, which leads to low simulation efficiency if the fine discretization is used in the whole simulation domain. Therefore, we propose an adaptive particle refinement scheme for PD. In our method, the refinement process only happens in the region near the crack path to increase the resolution with slight extra simulation cost. In this section, we will firstly propose two activation criteria to locate the refinement part. Then, we propose a refinement method by directly splitting a parent particle into child particles with the consideration of its deformation

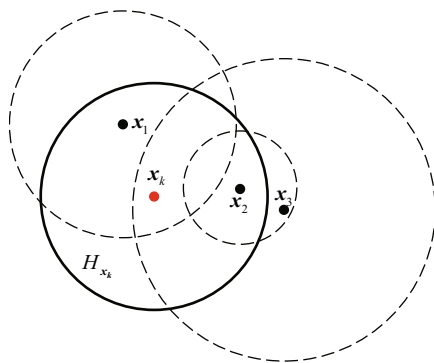


Fig. 2 Dual-horizon Peridynamics

3.1 Criterion for the activation of the refinement

In our methods, two activation criteria are adopted to locate the refinement part during the simulation. The first one is the critical damage criterion. If any particle x_k satisfies

$$\phi_k > \phi_c, \tag{15}$$

it will be refined, where ϕ_c is the critical damage value.

The second activation criteria is to locate the damage inside a single particle x_k . If any particle x_k satisfies

$$\min\{\epsilon_{xx}, \epsilon_{yy}, \epsilon_{zz}\} > 1 + \alpha s_c, \tag{16}$$

where $\alpha < 1$ is a prescribed positive constant, $\epsilon_{xx}, \epsilon_{yy}, \epsilon_{zz}$ are the accumulated strain in x, y, z direction of particle x_k determined by

$$\epsilon_{ii} = \frac{\sum_{x_j \in H_k} \mu_{kj} \frac{(u_j - u_k) \cdot n_i}{(x_j - x_k)} V_j}{\sum_{x_j \in H_k} \mu_{kj} V_j}, \tag{17}$$

where n_i is the unit normal vector along i -th direction. The satisfaction of Eq. (16) means that the crack propagation path may pass across the material domain represented by particle x_k , so the particle x_k needs to be refined to obtain a precise crack propagation path.

3.2 Particle refinement

In our particle refinement scheme, the properties of the refined child particles are only related to their ‘‘parent’’ coarse particle without requiring any information from their adjacent particles. Figures 3 and 4 show the basic idea of our refinement scheme in 2D and 3D cases. Here we only present the detailed refinement scheme for 3D case, and the refinement scheme for 2D case can be obtained similarly. As shown in Fig. 4, in our refinement scheme, when a coarse particle satisfy any refinement criteria presented in Sect. 3.1, it is split into several refined particles (8 particles in 3D case).

By considering the deformation of the parent particle x_k , the position of its i -th child particle x_k^i in the current configuration can be written as

$$y_k^i = y_k + \left[\frac{(1 + \epsilon_{xx})}{2} \Delta_k \xi^i, \frac{(1 + \epsilon_{yy})}{2} \Delta_k \eta^i, \frac{(1 + \epsilon_{zz})}{2} \Delta_k \zeta^i \right], \tag{18}$$

where $\xi^i, \eta^i, \zeta^i = \pm 1$, Δ_k is the initial particle length of particle x_k . And the position vector in reference configuration can be written as

$$x_k^i = x_k + \left[\frac{1}{2} \Delta_k \xi^i, \frac{1}{2} \Delta_k \eta^i, \frac{1}{2} \Delta_k \zeta^i \right]. \tag{19}$$

One of the major simulation cost of the particle refinement method in PD is the update of the physical properties and the

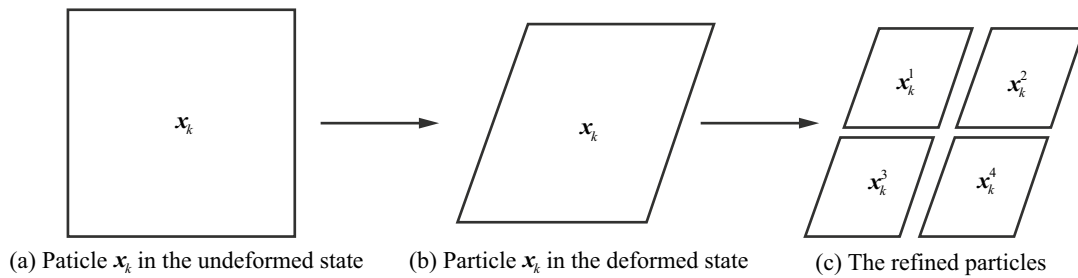


Fig. 3 The refinement scheme for 2D cases

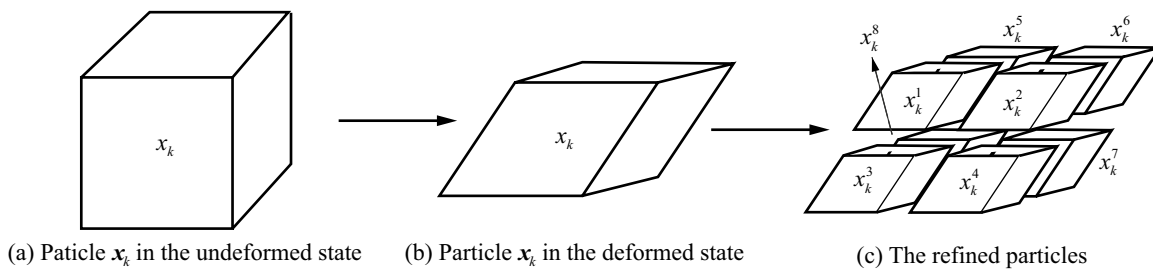


Fig. 4 The refinement scheme for 3D cases

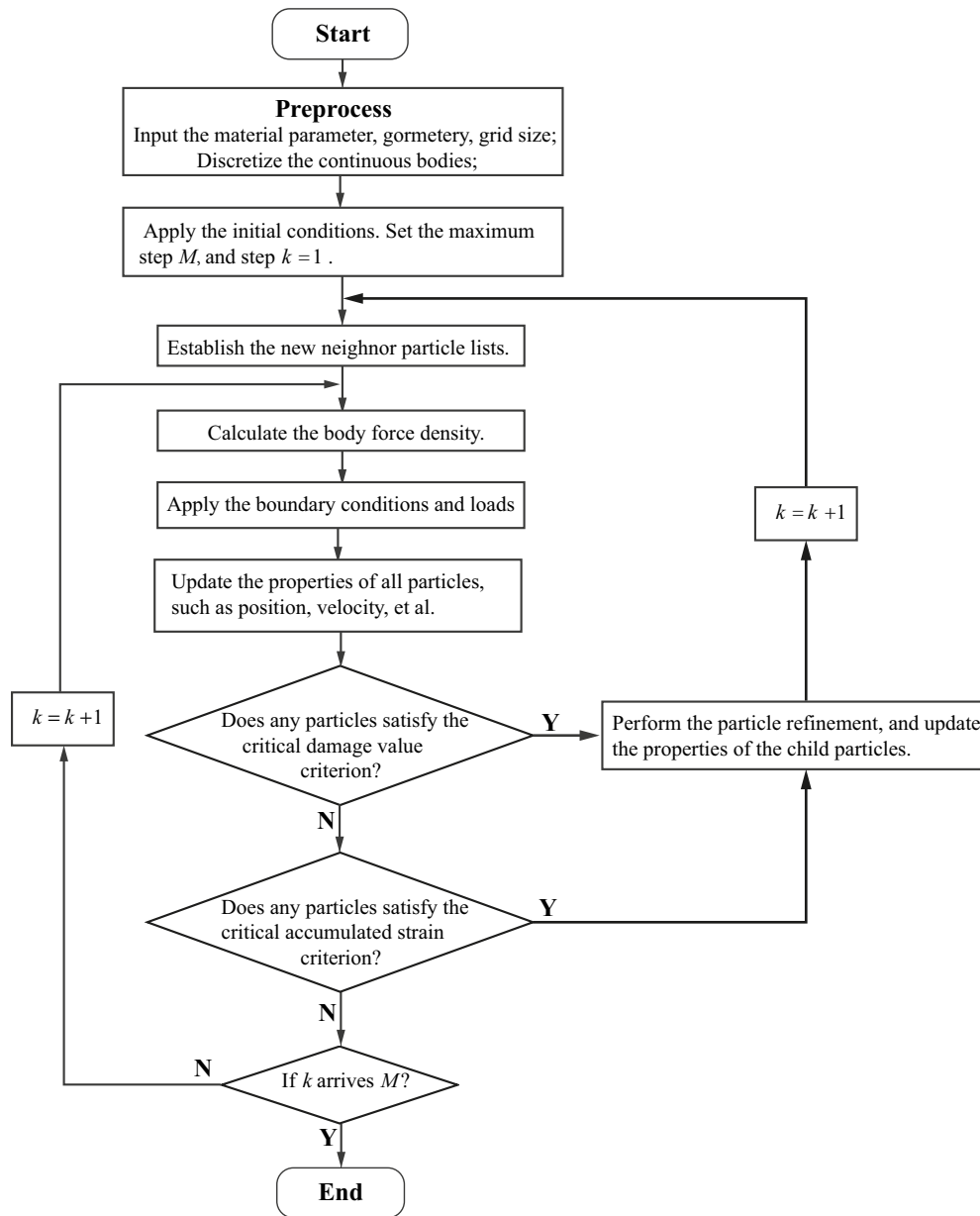


Fig. 5 The flow chart of the adaptive refinement method based on dual-horizon ordinary state-based PD

neighbor particle list of the child particles \mathbf{x}_k^i . In our particle refinement scheme, the properties of the child particle are only related to its parent particle. The velocity of the child particles \mathbf{x}_k^i is equal to the velocity of its parent particle, and the mass and volume of the child particles \mathbf{x}_k^i equal to the 1/8 of the values of its parent particle. Because the horizon size of the child particles \mathbf{x}_k^i is 1/2 of its parent particle, the traditional horizon H_k^i and a dual horizon $H_k^{i'}$ of the child particles \mathbf{x}_k^i can be easily obtained. We define the following collection

$$H_{k,s} = H_k \cup \mathbf{x}_k^i \quad (20)$$

$$H_{k,s}' = H_k' \cup \mathbf{x}_k^i \quad (21)$$

The traditional horizon H_k^i and a dual horizon $H_k^{i'}$ of the child particles \mathbf{x}_k^i is the subset of $H_{k,s}$ and $H_{k,s}'$, which can be obtained by

$$H_k^i = \{\mathbf{x}_j | \mathbf{x}_j \in H_{k,s} \text{ and } \|\mathbf{x}_k^i - \mathbf{x}_j\| < \delta_k^i\} \quad (22)$$

Fig. 6 A rectangular plate under uniaxial tension

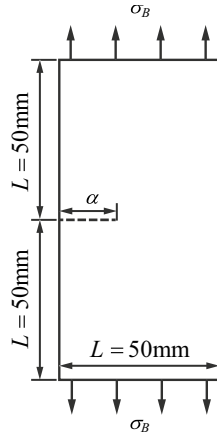


Table 1 The material parameters for crack-opening problem

$E(\text{GPa})$	ν	$\rho(\text{kg/m}^3)$
200	1/3	7850

$$H'_k = \{x_j | x_j \in H'_{k,s} \text{ and } x_k \in H_j\} \tag{23}$$

Therefore, the update of the information of the child particles x'_k is much more efficient than the methods in the literature [28, 29].

To summarize, the flowchart of the proposed adaptive particle refinement scheme for PD is shown in Fig. 5. The details of numerical implementation of the adaptive refinement process are as follow. Firstly, the following steps are performed prior to the first time step:

- (1). Discretize the continuum body by a set of particles with an uniform particle size Δ and an uniform horizon size δ ;
- (2). Set the physical properties of the particles, such as mass, volume;

Table 2 The crack-opening distance and error of different method

α/L	0.1	0.2	0.3	0.4	0.5
Analytic Formula	1.5398 μm	3.5984 μm	6.9257 μm	12.9145 μm	24.6169 μm
Coarse Discretization	1.5882 μm (3.14%)	3.6909 μm (2.57%)	7.2174 μm (4.21%)	13.3498 μm (3.37%)	24.9987 μm (1.55%)
Adaptive Discretization ($\delta_2 = 0.5\delta_1$)	1.5741 μm (2.23%)	3.6612 μm (1.75%)	7.0860 μm (2.31%)	13.2261 μm (2.41%)	24.8786 μm (1.06%)
Fine Discretization	1.5578 μm (1.17%)	3.6314 μm (0.92%)	7.0097 μm (1.21%)	13.0961 μm (1.41%)	24.7853 μm (0.68%)

Table 3 The crack-opening distance and relative error of different horizon sizes

α/L	0.1	0.2	0.3	0.4	0.5
Analytic Formula	1.5398 μm	3.5984 μm	6.9257 μm	12.9145 μm	24.6169 μm
Adaptive Discretization $\delta_2 = 0.5\delta_1$	1.5741 μm (2.23%)	3.6612 μm (1.75%)	7.0860 μm (2.31%)	13.2261 μm (2.41%)	24.8786 μm (1.06%)
Adaptive Discretization $\delta_2 = 1.0\delta_1$	1.5709 μm (2.02%)	3.6609 μm (1.74%)	7.0821 μm (2.26%)	13.2197 μm (2.36%)	24.8717 μm (1.03%)

- (3). Set the pre-set-cracks and calculate the damage value of all particles.
- (4). Determine the particles to be refined by employing the critical damage value criterion Eq. (15);
- (5). Update the neighbor particle list of the traditional horizon $H_k = \{x_j | (x_j - x_k)^2 < \delta_k^2\}$ and the dual horizon $H'_k = \{x_j | x_k \in H_j\}$ of each particle;

For each time step i , the following steps are performed:

- (1). Compute the internal force $f^i_{k,int}$ and the external force $f^i_{k,ext}$ of each particle

$$f^i_{k,int} = \sum_{x_j \in H_k} [\mathbf{t}_{kj}(\mathbf{u}_j - \mathbf{u}_k, \mathbf{x}_j - \mathbf{x}_k, t) - \mathbf{t}_{jk}(\mathbf{u}_k - \mathbf{u}_j, \mathbf{x}_k - \mathbf{x}_j, t)] V_j V_k \tag{24}$$

$$f^i_{k,ext} = m(\mathbf{x}_k) \mathbf{b}(\mathbf{x}_k, t) \tag{25}$$

- (2). Update the velocity and displacement of each PD particle by

$$\mathbf{v}_k^{i+1/2} = \mathbf{v}_k^{i-1/2} + \Delta t \frac{f^i_{k,int} + f^i_{k,ext}}{m_k}, \tag{26}$$

$$\mathbf{y}_k^{i+1} = \mathbf{y}_k^i + \Delta t^{i+1/2} \mathbf{v}_k^{i+1/2}, \tag{27}$$

and apply the displacement and velocity boundary condition on boundary particles by

$$\mathbf{u}_k^{i+1} = \bar{\mathbf{u}}_k^{i+1}, \mathbf{x}_k \in \Gamma_u \tag{28}$$

$$\mathbf{v}_k^{i+1/2} = \bar{\mathbf{v}}_k^{i+1/2}, \mathbf{x}_k \in \Gamma_v \tag{29}$$

where $\bar{\mathbf{u}}_k^{i+1}$ and $\bar{\mathbf{v}}_k^{i+1/2}$ denote the prescribed displacement and velocity, respectively, Γ_u and Γ_v denote the

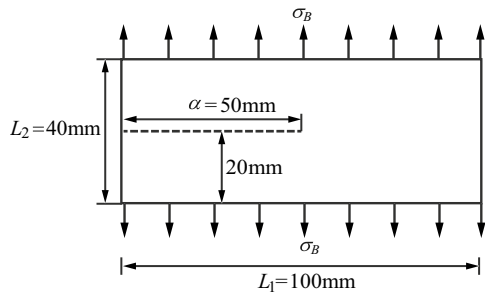


Fig. 7 A plate with a central crack under transient tensile loading

Table 4 The material parameters for dynamic crack branching

$E(\text{GPa})$	ν	$\rho(\text{kg/m}^3)$	$G_c(\text{J/m}^2)$
32	0.2	2450	3

particle set of prescribed displacement and velocity boundaries, respectively;

- (3). Update the damage value based on Eq. (14) and the accumulated strain based on Eq. (17) of all particles;
- (4). Perform the particle refinement process if a particle x_k satisfies any one of the critical damage value criterion Eq. (15) and critical accumulated strain criterion Eq. (16). Update the position of the child particles x_k^j in the current configuration and the original configuration by Eqs. (18) and (19), respectively. Update the mass, volume, velocity, horizon size of the child particles by

$$\begin{aligned}
 m_k^j &= d_g m_k \\
 V_k^j &= d_g V_k \\
 \mathbf{v}_k^{i+1/2,j} &= \mathbf{v}_k^{i+1/2} \\
 \delta_k^j &= 0.5 \delta_k
 \end{aligned} \quad (30)$$

where $d_g = 0.25$ in 2D cases and $d_g = 0.125$ in 3D cases.

- (5). Update the neighbor particle list of the traditional horizon H_k^j of the child particles x_k^j by searching in the traditional horizon of the parent particle x_k .

4 Numerical applications

All examples in this paper are simulated by a PC with one Intel(R) core(TM) i7-13900K CPU @ 3.40 GHz.

4.1 Crack-opening problem

In this section, a rectangular plate under uniaxial tension with a single edge crack is studied. The geometric setting of this problem is shown in Fig. 6. The tensile stress $\sigma_B = 10\text{MPa}$ is applied on the top and bottom surfaces of the plate. The material parameters are listed in Table 1. In this simulation, the square plate is initially discretized into a set of particles with spacing $\Delta_1 = 1\text{mm}$ in coarse discretization and $\Delta_2 = 0.5\text{mm}$ in fine discretization, and the horizon size $\delta_1 = 3.015\Delta_1$. The parameters used in the criterion for the activation of the refinement in Eqs. (15) and (16) are set as $\phi_c = 0.4$, $\alpha = 0.5$.

Irwin et al. [32] theoretically studied this problem and gave the analytic formula of the crack-opening displacement

$$d_0 = \frac{4\sigma_B \alpha}{E} f\left(\frac{\alpha}{L}\right) \quad (31)$$

where

$$f\left(\frac{\alpha}{L}\right) = \frac{1.46 + 3.42(1 - \cos(\pi\alpha/2L))}{\cos^2(\pi\alpha/2L)} \quad (32)$$

To obtain the quasi-static results and neglect the effect of dynamic loading, the adaptive dynamic relaxation method proposed by Madenci [33] is used. The Simulation results of all three discretization schemes are shown in Table 2. The results of all three discretization schemes show great agreement with the analytic solution. In the adaptive refinement method, the adaptive refinement process only occurs around the crack path, and have better grid resolution compared to the coarse discretization. Therefore, we can obtain a better result by using the proposed adaptive refinement method with only slight extra simulation cost.

To study the effect of different horizon sizes in the adaptive refinement method, two different horizon sizes of child particle, $\delta_2 = 0.5\delta_1$, $1.0\delta_1$, are used to simulate this problem. The results of different horizon sizes are shown in Table 3. As mentioned by Oterkus et al. [34], a better agreement is obtained for a constant horizon size in the solution domain, and the difference is tiny in the crack-opening problem. However, in the adaptive refinement method, the refine process usually happens near the crack surface, and the large horizon size near the surface may cause a more serious side effect which may leads to a worse simulation result. And a constant horizon size leads to a poor simulation efficiency which against the original intention of the dual-horizon PD. Therefore, in the following numerical application, we set $\delta_i = 3.015\Delta_i (i = 1, 2)$ [25].

4.2 Dynamic crack branching

In this section, a dynamic crack branching process of a central crack in a plate under transient tensile loading is studied.

Fig. 8 Dynamic crack branching with different discretization: **a** Coarse discretization; **b** Fine discretization; **c** Adaptive refinement

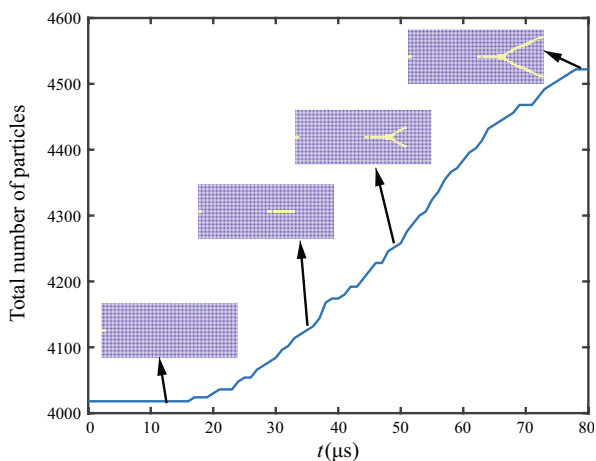
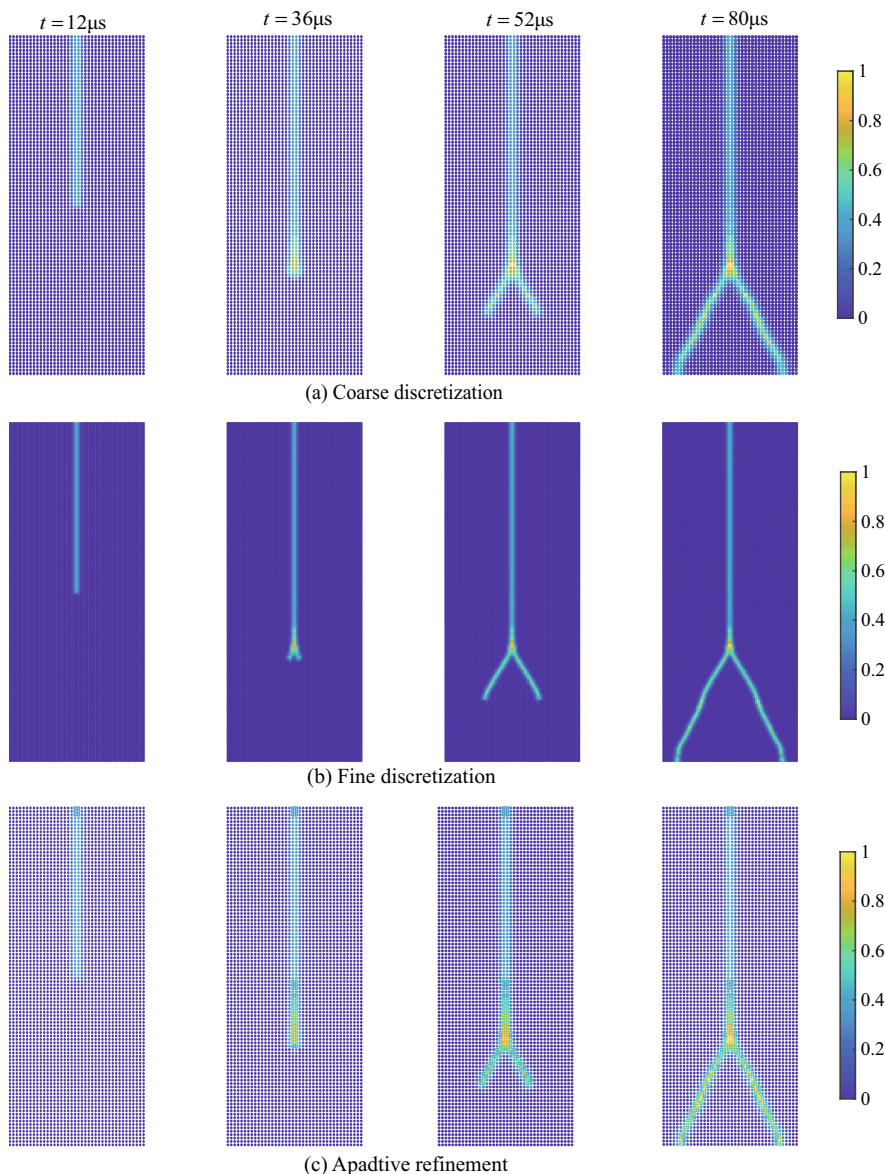


Fig. 9 Evolution of the total number of particles in Case 1

As shown in Fig. 7, the specimen’s length $L_1 = 100\text{mm}$, width $L_2 = 40\text{mm}$ and thickness $t = 1\text{mm}$. The length of the initial crack equals to 50mm . The tensile stress is applied continuously on the top and bottom surfaces of the plate. The material parameters are listed in Table 4. In this simulation, the square plate is initially discretized into a set of particles with spacing $\Delta_1 = 1\text{mm}$ in coarse discretization and $\Delta_2 = 0.5\text{mm}$ in fine discretization, and the horizon size $\delta_i = 3.015\Delta_i (i = 1, 2)$. The time step is set to $\Delta t = 1 \times 10^{-8}\text{s}$ for all the cases. This problem has been experimentally investigated by Sharon et al. [35] and Fliss et al. [36] and numerically studied by Belytschko et al. [37] by XFEM and Borden et al. [38] by phase field method. These experimental and numerical studies have shown that the crack will branch in the process of rapid propagation.

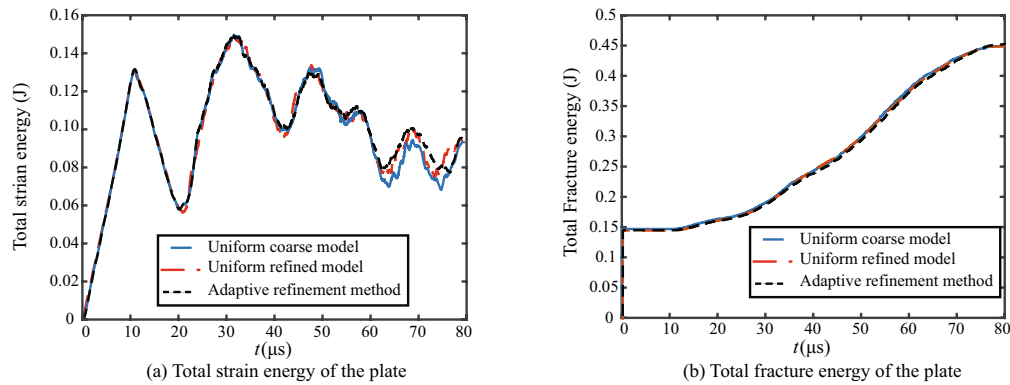


Fig. 10 Energy curves in Case 1 **a** Total elastic strain energy; **b** Total fracture energy

Table 5 Simulation cost comparison for Case 1

	Total particles	Total simulation time for physical simulation time 80 μs	Total refinement time
Coarse Discretization	4000	252 s	\
Adaptive Discretization	4000–4522	311 s	9 s
Fine Discretization	16,000	1441s	\

In this study, two cases with different tensile loads are investigated: (1) Case 1: $\sigma_B = 1\text{MPa}$; (2) Case 2: $\sigma_B = 2\text{MPa}$. The parameters used in the criterion for the activation of the refinement in Eqs. (15) and (16) are set as $\phi_c = 0.4$, $\alpha = 0.5$.

Figure 8 shows the evolution of the particle damage value obtained with the coarse discretization, fine discretization and adaptive refinement method in Case 1. In all three discretization schemes, the occurrence of a branched crack is observed at approximately $t = 35\mu\text{s}$ and the crack tip reaches at the material boundary at approximately $t = 80\mu\text{s}$, which agree well with the reported simulation results [38, 39]. Furthermore, the crack branching path and the distance between two crack tips near the material boundary is similar to the reported results [38, 39].

Figure 9 illustrates the evolution of the total particle numbers and the particle type in the adaptive refinement method. The yellow particles are the refined particles with spacing $\Delta_2 = 0.5\text{mm}$ and the blue particles are the coarse particles with spacing $\Delta_1 = 1\text{mm}$. The adaptive refinement process only occurs around the crack propagation path and the left end of the original crack, which will lead to slight particle number increase and slight extra computational cost.

Figure 10 plots the evolution of the total strain energy and total fracture energy of the plate with different discretization schemes, which all agree well with the reported simulation results [38, 39]. No obvious difference can be observed between all three discretization schemes because of the low tensile load value.

Table 5 compares the computational cost of all three discretization schemes. The extra simulation cost for particle refinement of the proposed adaptive refinement method is small compared to other methods [28, 29], which makes the proposed adaptive refinement method very efficient.

Figure 11 shows the evolution of the particle damage value obtained with the coarse discretization, fine discretization and adaptive refinement method in Case 2. Different from Case 1, the results of the three discretization schemes show great difference. In the coarse discretization, the fake damage will happen at the middle of two crack branch paths and the top and bottom surfaces of the plate due to the low grid resolution. However, the results with fine discretization and adaptive refinement method have no such phenomenon.

Similar to Figs. 9, 12 plots the evolution of the total number of particles and the particle type in the adaptive refinement method. The adaptive refinement process only occurs around the crack propagation path and the left end of the original crack, which will lead to slight particle number increase and slight extra computational cost. However different from Case 1, we can obtain much more accurate results by using the adaptive refinement method with slight extra computational cost in Case 2.

Figure 13 shows the evolution of the total strain energy and total fracture energy of the plate obtained with coarse discretization, fine discretization and adaptive refinement method. As shown in Fig. 13b, all three discretization schemes can catch the crack growth starting and crack branching starting process, so that all three discretization

Fig. 11 Dynamic crack branching with different discretization: **a** Coarse discretization; **b** Fine discretization; **c** Adaptive refinement

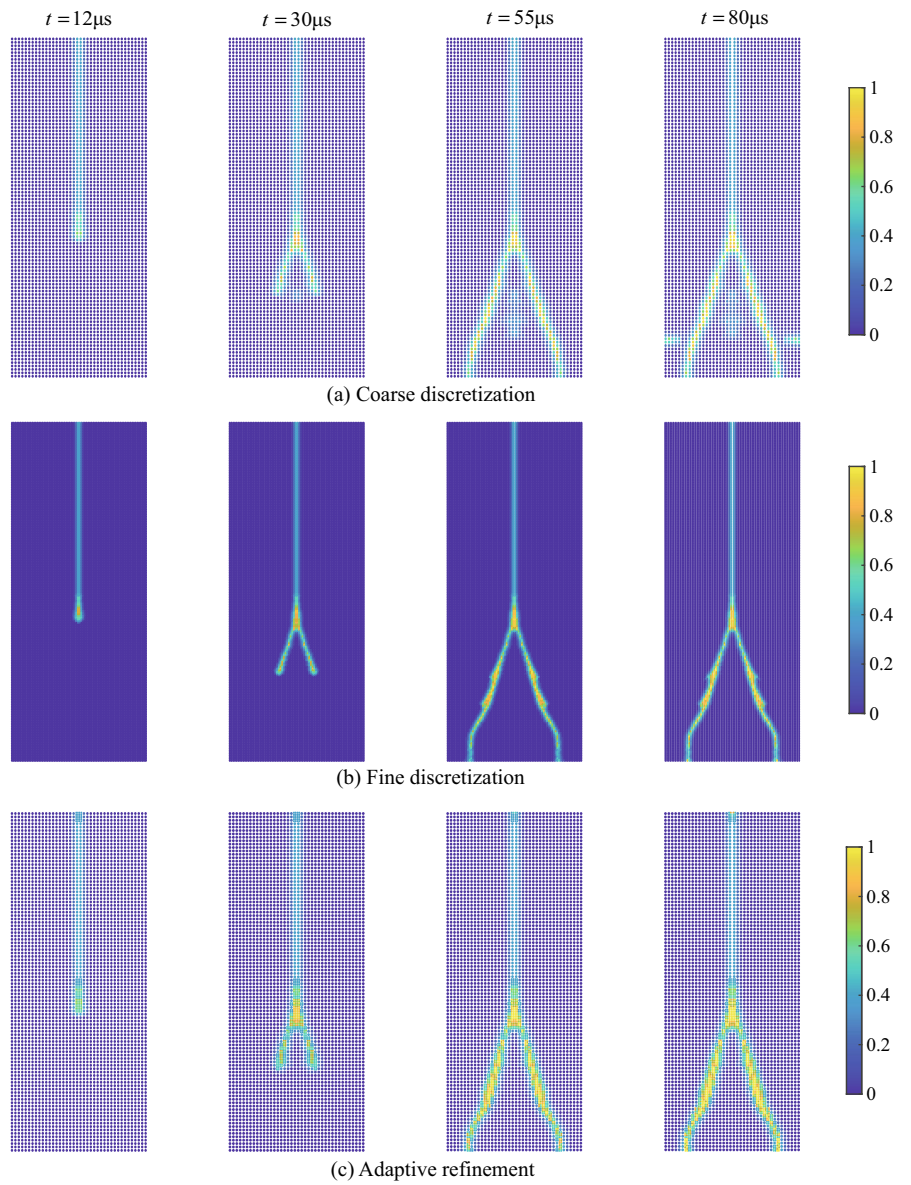
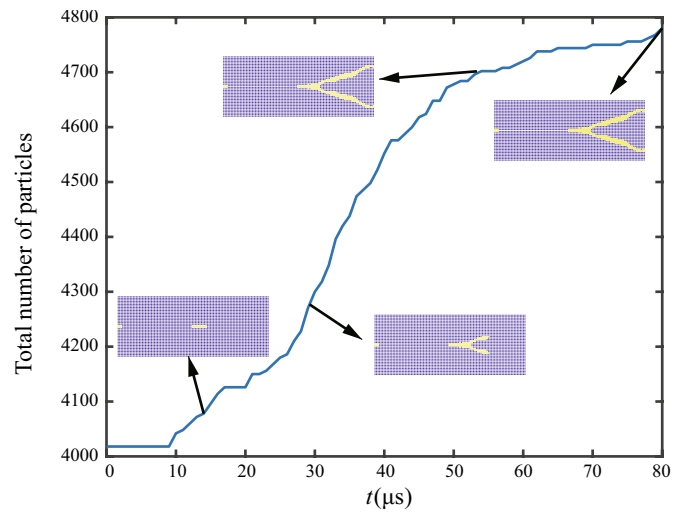


Fig. 12 Evolution of the total number of particles in Case 2



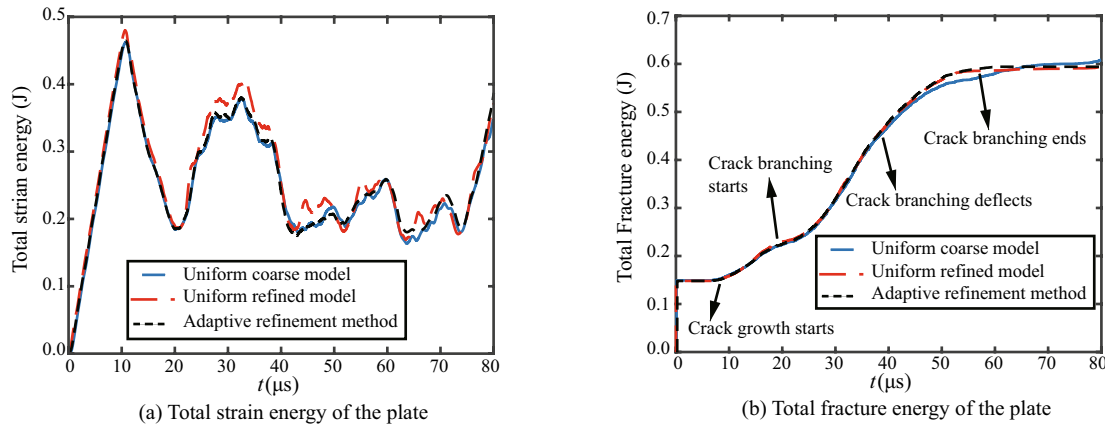


Fig. 13 Energy curves in Case 2: **a** Total elastic strain energy; **b** Total fracture energy

Table 6 Simulation cost comparison for Case 2

	Total particles	Total simulation time for physical simulation time 80 μs	Total refinement time
Coarse discretization	4000	248 s	\
Adaptive discretization	4000–4783	309 s	13 s
Fine discretization	16,000	1411 s	\

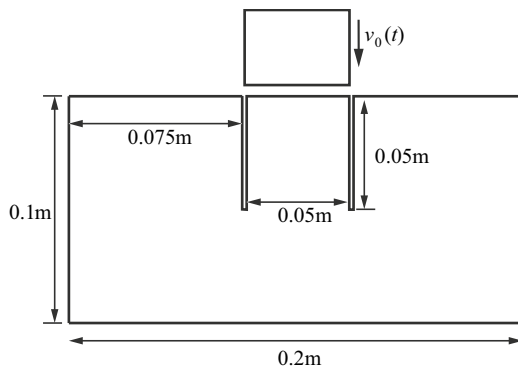


Fig. 14 Kalthoff-Winkler's experimental setup

Table 7 The material parameters for Kalthoff-Winkler's experiment

E (GPa)	ν	ρ (kg/m ³)	G_c (J/m ²)
190	0.25	8000	22170

schemes have the similar total energy curves before $t = 40\mu s$. However, the crack branching path will deflect in the results obtained with the fine discretization and adaptive refinement method, which can not be caught with the coarse discretization, making the low increase rate of the total fracture energy after $t = 40\mu s$. Furthermore, the crack branching

process will end at $t = 55\mu s$, so the total fracture energy curve obtained by the fine discretization and adaptive refinement method almost stop increasing after $t = 55\mu s$. However, due to the persistent fake crack growth at the middle of two crack branch paths and the top and bottom surfaces of the plate, the total fracture energy curve obtained by the coarse discretization still keep increasing after $t = 55\mu s$.

Table 6 compares the computational cost of all three discretization schemes, which shows that we can obtain a result similar to the fine discretization by using the proposed adaptive refinement method with only slight extra simulation cost.

4.3 Kalthoff experiment

Kalthoff Windler Experiment [40–42] is an classical benchmark for dynamic crack growth simulation. As shown in Fig. 14, a rectangular steel plate with two parallel preset cracks is stricken by a steel impactor. The material parameters of the plate are listed in Table 7.

The thickness of the specimen is 0.01m. The impact loading is imposed by applying an initial velocity of $v_0 = 16.5\text{m/s}$ to the first three layers of particles in the domain (see Fig. 14), and all the other boundaries are free. In this simulation, the square plate is initially discretized into a set of particles with spacing $\Delta_1 = 2\text{mm}$ in coarse discretization and $\Delta_2 = 1\text{mm}$ in fine discretization with the horizon

Fig. 15 Kalthoff experiment crack simulation with different discretization: **a** Coarse discretization; **b** Fine discretization; **c** Adaptive refinement

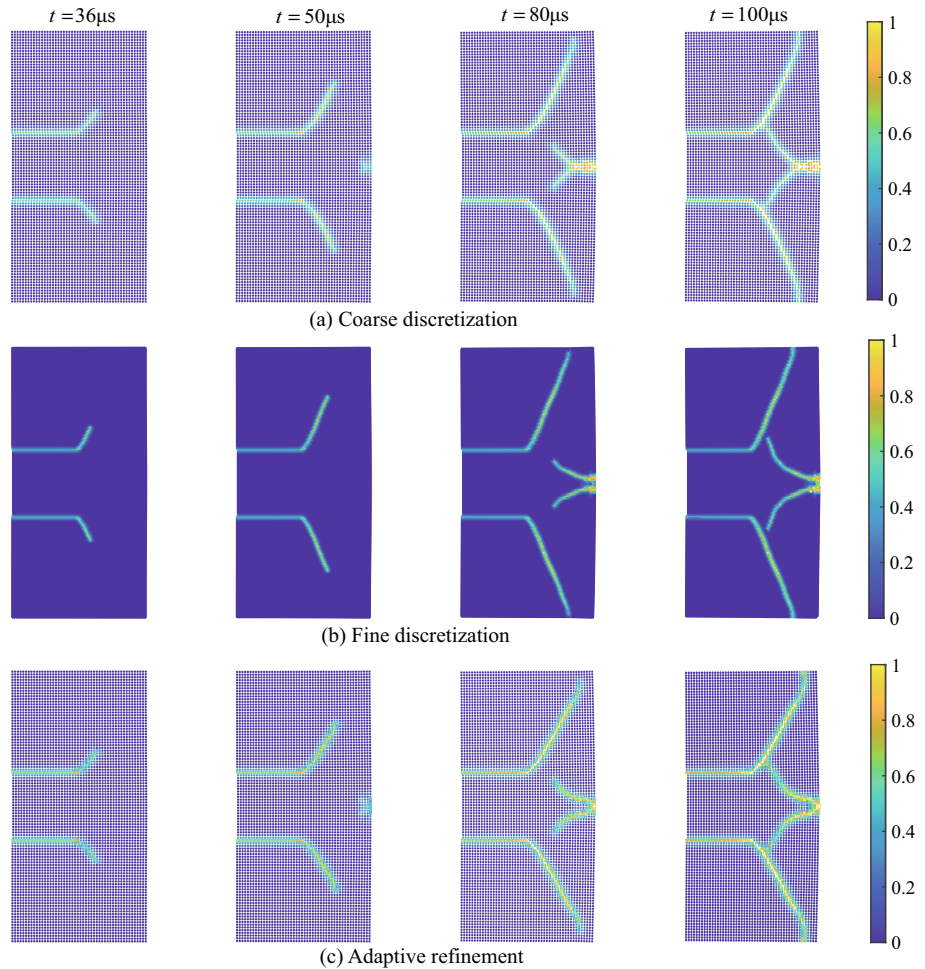


Table 8 Simulation result comparison

	Total particles	Deflecting angle	Total simulation time for physical simulation time 100 μs	Total refinement time
Coarse discretization	5000	61.80°	394 s	\
Adaptive discretization	5000–6038	60.88°	522 s	16 s
Fine discretization	20,000	66.06°	2127 s	\

size $\delta_i = 3.015\Delta_i$. The time step is set to $\Delta t = 1 \times 10^{-8}$ s. The parameters in criterion for the activation of the refinement in Eqs. (15) and (16) are set as $\phi_c = 0.4, \alpha = 0.5$.

Figure 15 show the evolution of the particle damage value obtained with coarse discretization, fine discretization and adaptive refinement method. Two crack propagation process are observed in the simulation: (1) Two primary fractures originating from the preset cracks; (2) A secondary fracture generated at the right side of the plate. The similar phenomenon is observed in the simulation of Belyschko’s [37] and Dipasquale’s [29]. All three discretization schemes can catch the propagation of the primary fracture

at about $t = 24\mu\text{s}$. The crack path direction of the primary fracture is almost straight, and the deflecting angle of the crack propagation with respect to the original crack direction obtained by different methods are shown in Table 8. The deflecting angles obtained by all three discretization schemes are close to the experiment results [41, 42]. As shown in Fig. 16, the crack path of the primary fracture of all three discretization schemes are close to the results of PFMPM [43] and XFEM [37]. However, the evolution of the secondary fracture obtained by three discretization schemes is obviously different. In the coarse discretization, a single secondary crack firstly appears at about $t = 50\mu\text{s}$ and then propagates. when $t = 66\mu\text{s}$, the single secondary crack

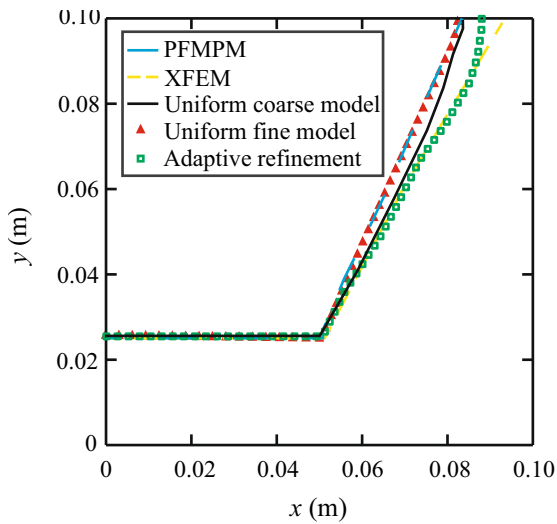
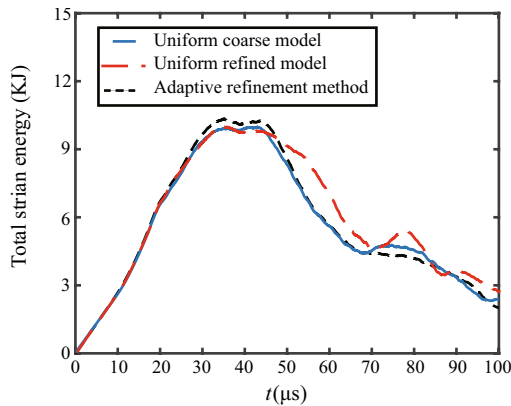
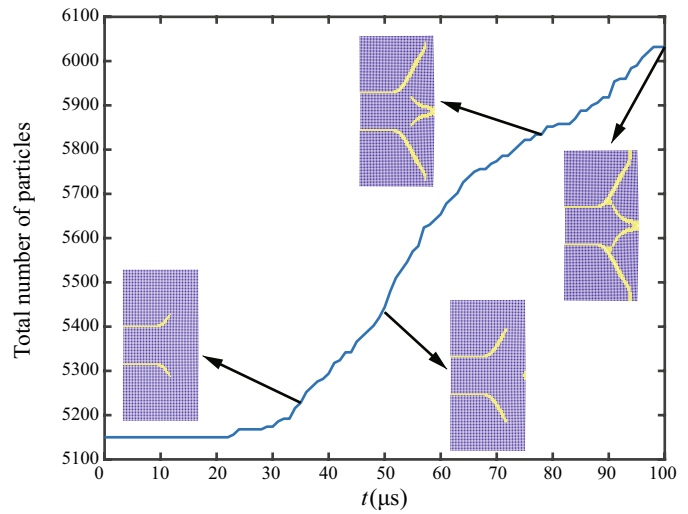
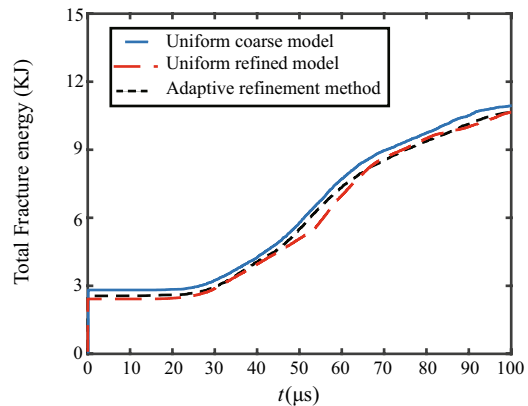


Fig. 16 The crack path of the primary fracture

Fig. 17 Evolution of the total number of particles with adaptive refinement



(a) Total strain energy of the plate



(b) Total fracture energy of the plate

Fig. 18 Energy curves: a Total elastic strain energy; b Total fracture energy

branches into two cracks and keeps propagating. However, in the fine discretization and adaptive refinement method, two secondary cracks appear directly at about $t = 50\mu\text{s}$ and keep propagating. when $t = 80\mu\text{s}$, two secondary cracks have a slight deflect and keep propagating straight. It is probably caused by the low grid resolution of the coarse discretization near the right end of the plate, which makes it difficult to separate two different secondary cracks at the beginning.

Figure 17 plots the evolution of the total number of particles and the particle type in the adaptive refinement method. The adaptive refinement process only occurs around the crack propagation path, which leads to slight particle number increase and slight computational cost increase, as shown in Table 8.

Figure 18 shows the evolution of the total strain energy and total fracture energy of the plate obtained with coarse discretization, fine discretization and adaptive refinement method. The tendency of the total strain energy curve and the total fracture energy curve are similar in all three discretization schemes. However, due to the more accurate

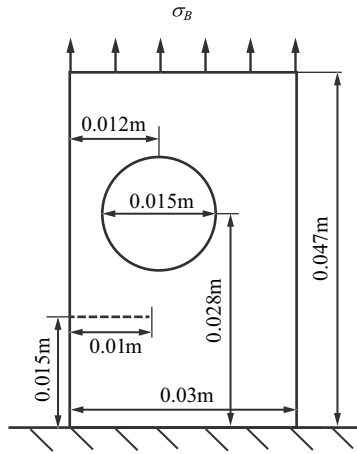


Fig. 19 Pre-cracked plate with a hole

Table 9 The material parameters for traction of Pre-cracked plate with a hole

$E(\text{GPa})$	ν	$\rho(\text{kg/m}^3)$	$G_c(\text{J/m}^2)$
71.4	0.33	2700	1000

secondary crack propagation process, the total fracture energy curve obtained with the adaptive refinement method

are more close to that of the fine discretization than the coarse discretization.

4.4 Traction of pre-cracked plate with a hole

As shown in Fig. 19, a rectangular plate with a pre-set crack and a circular hole under tensile load is studied in this section. The tensile load $\sigma_B = 26\text{MPa}$ is applied on the top edge of the plate, and the bottom edge of the plate is fixed. The material parameters of the plate are listed in Table 9. In this simulation, the square plate is initially discretized into a set of particles with spacing $\Delta_1 = 0.5\text{mm}$ in coarse discretization and $\Delta_2 = 0.25\text{mm}$ in fine discretization with the horizon size $\delta_i = 3.015\Delta_i$. The time step is set to $\Delta t = 1 \times 10^{-8}\text{s}$, and the parameters in criterion for the activation of the refinement in Eqs. (15) and (16) are set as $\phi_c = 0.4, \alpha = 0.5$.

Figure 20 show the evolution of the nodal value of damage with coarse discretization, fine discretization and adaptive refinement method. All the three discretization can capture the similar crack propagation process of the pre-set crack below the hole, which grows at about $t = 20\mu\text{s}$ and ends at about $t = 30\mu\text{s}$. And the crack deflecting angle is also similar between all the three discretization schemes. However, because the orthogonal discretization are used in all the three discretization schemes, the resolution of the boundary is poor near the hole, which will cause 2 fake cracks growing from the hole boundary

Fig. 20 Traction of pre-cracked plate with different discretization: a Coarse discretization; b Fine discretization; c Adaptive refinement

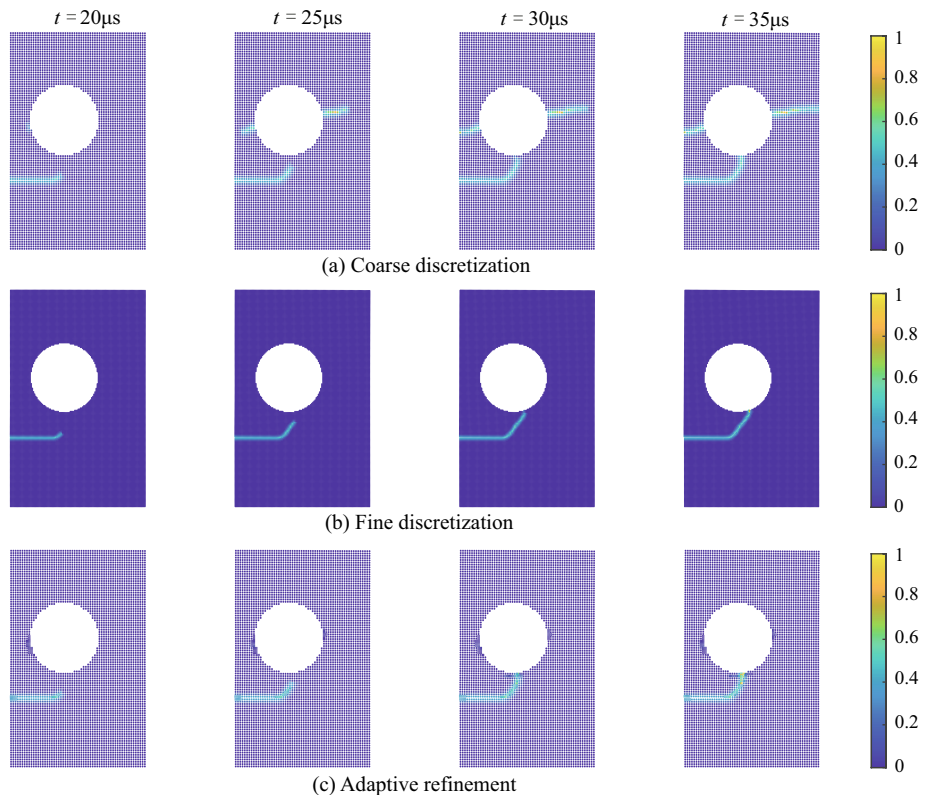


Fig. 21 Evolution of the total number of particles with adaptive refinement

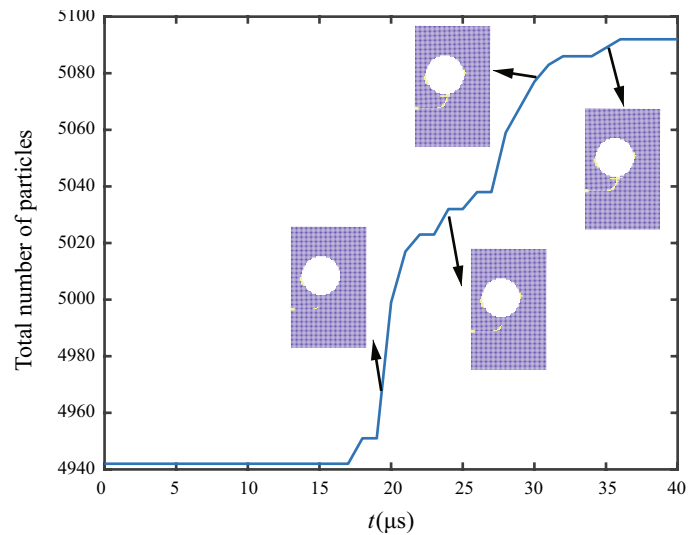
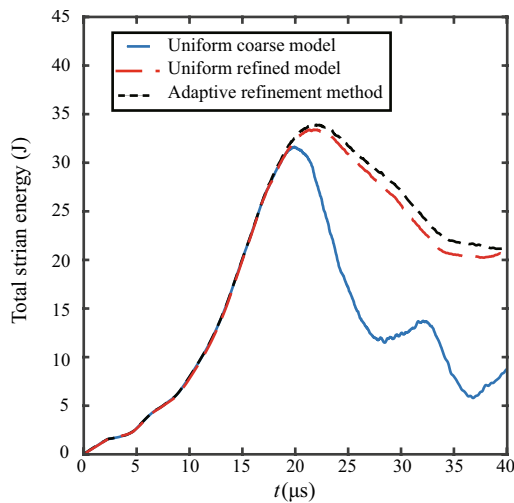
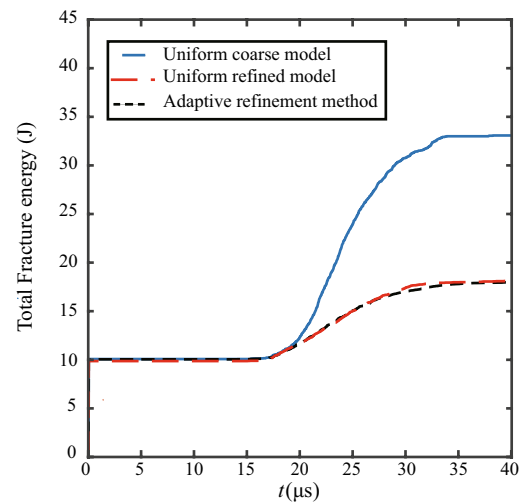


Table 10 Simulation cost comparison

	Total particles	Total simulation time for physical simulation time 40 μ s	Total refinement time
Coarse Discretization	4924	155 s	\
Adaptive Discretization	4942–5092	164 s	3 s
Fine Discretization	19,732	837 s	\



(a) Total strain energy of the plate



(b) Total fracture energy of the plate

Fig. 22 Energy curves: **a** Total elastic strain energy; **b** Total fracture energy

with the coarse refinement. Using the proposed adaptive refinement method, the fake cracks disappear and similar results to the fine discretization are obtained.

Figure 21 shows the evolution of the total number of particles and the particle type in the adaptive refinement method. The adaptive refinement process only occurs

around the crack propagation path and the hole boundary, which lead to slight particle number increase and slight computational cost increase, as shown in Table 10. The refinement area near the hole boundary is much smaller than that in the results of Dipasquale's [29].

Figure 22 plots the evolution of the total strain energy and total fracture energy of the plate obtained with coarse discretization, fine discretization and adaptive refinement method. The tendency of the total strain energy curve and the total fracture energy curve are similar between the fine discretization and the adaptive refinement method. However, due to the fake crack growth, the fracture energy of the plate obtained with the coarse discretization rapidly increase, and the strain energy rapidly decrease after the crack growth beginning, compared to the fine discretization.

5 Conclusion

In this paper, a novel efficient adaptive refinement method is proposed based on the ordinary state-based PD for both 2D and 3D dynamic crack propagation problems. Two refinement criteria based on the damage value and the critical accumulated strain are proposed to activate the adaptive refinement process near the crack area. In our particle refinement scheme, the properties of the refined child particles are only related to their parent particle, which does not require any information from adjacent particles. And the position of the child particles in the current configuration can be calculated directly by the defined accumulated strain of their parent particle, as introduced in Sect. 3.2. Because of the convenience of the property and neighbor list update of the refined particles, the proposed adaptive refinement method has high simulation efficiency in the refinement process. The examples presented in the paper show that the proposed adaptive refinement can correctly capture the complex crack propagation process and reduce the fake crack growth with a little extra simulation cost, compared to the coarse discretization. Results are in good agreement with those obtained with other computational methods or experimental tests. Although 2D numerical examples are only considered in this paper, the proposed method can be easily applied in both 2D and 3D cases due to its simplicity, compared to the existing methods [28, 29].

Data availability The data that support the findings of this study are available from the corresponding author upon reasonable request.

References

- Xu XP, Needleman A (1996) Numerical simulations of dynamic interfacial crack growth allowing for crack growth away from the bond line. *Int J Fract* 74(3):253–275. <https://doi.org/10.1007/BF00033830>
- Mos N, Dolbow J, Belytschko T (1999) A finite element method for crack growth without remeshing. *Int J Numer Meth Eng* 46:131–150. [https://doi.org/10.1002/\(SICI\)1097-0207\(19990910\)46:1<131::AID-NME726>3.0.CO;2-J](https://doi.org/10.1002/(SICI)1097-0207(19990910)46:1<131::AID-NME726>3.0.CO;2-J)
- Carpinteri A, Ferro G, Ventura G (2001) An augmented lagrangian element-free (ALEF) approach for crack discontinuities. *Comput Methods Appl Mech Eng* 191(8–10):941–957. [https://doi.org/10.1016/S0045-7825\(01\)00288-2](https://doi.org/10.1016/S0045-7825(01)00288-2)
- Krysl P, Belytschko T (1999) The element free galerkin method for dynamic propagation of arbitrary 3-d cracks. *International Journal for Numerical Methods in Engineering* 44. [https://doi.org/10.1002/\(SICI\)1097-0207\(19990228\)44:6<767::AID-NME524>3.0.CO;2-G](https://doi.org/10.1002/(SICI)1097-0207(19990228)44:6<767::AID-NME524>3.0.CO;2-G)
- Rao BN, Rahman S (2003) Mesh-free analysis of cracks in isotropic functionally graded materials. *Eng Fract Mech* 70(1):1–27. [https://doi.org/10.1016/S0013-7944\(02\)00038-3](https://doi.org/10.1016/S0013-7944(02)00038-3)
- Rabczuk T, Belytschko T (2004) Cracking particles: a simplified meshfree method for arbitrary evolving cracks. *Int J Numer Meth Eng* 61(13):2316–2343. <https://doi.org/10.1002/nme.1151>
- Nairn JA (2003) Material point method calculations with explicit cracks. *Comput Model Eng Sci* 4(6):649–664. <https://doi.org/10.3970/CMES.2003.004.649>
- Liang Y, Benedek T, Liu Y, Zhang X (2017) Material point method with enriched shape function for crack problems. *Comput Methods Appl Mech Eng* 322(aug.1):541–562. <https://doi.org/10.1016/j.cma.2017.05.012>
- Silling SA, Zimmermann M, Abeyaratne R (2003) Deformation of a peridynamic bar. *J Elast* 73(1):173–190. <https://doi.org/10.1023/B:ELAS.0000029931.03844.4f>
- Silling SA (2000) Reformulation of elasticity theory for discontinuities and long-range forces. *J Mech Phys Solids* 48(1):175–209. [https://doi.org/10.1016/S0022-5096\(99\)00029-0](https://doi.org/10.1016/S0022-5096(99)00029-0)
- Silling SA, Askari E (2005) A meshfree method based on the peridynamic model of solid mechanics. *Computers and Structures* 83. <https://doi.org/10.1016/j.compstruc.2004.11.026>
- Silling SA, Epton M, Weckner O, Xu J, Askari E (2007) Peridynamic states and constitutive modeling. *J Elast* 88(2):151–184. <https://doi.org/10.1007/s10659-007-9125-1>
- Foster JT, Silling SA, Chen WW (2010) Viscoplasticity using peridynamics. *Int J Numer Meth Eng* 81(10):1242–1258. <https://doi.org/10.1002/nme.2725>
- Amani J, Oterkus E, Areias P, Zi G, Nguyen-Thoi T (2016) A non-ordinary state-based peridynamics formulation for thermoplastic fracture. *Int J Impact Eng* 87:83–94. <https://doi.org/10.1016/j.ijimpeng.2015.06.019>
- Madenci E, Dorduncu M, Gu X (2019) Peridynamic least squares minimization. *Comput Methods Appl Mech Eng* 348:846–874. <https://doi.org/10.1016/j.cma.2019.01.032>
- Silling SA, Parks ML, Kamm JR, Weckner O, Rassaian M (2017) Modeling shockwaves and impact phenomena with eulerian peridynamics. *Int J Impact Eng* 107(sep.):47–57. <https://doi.org/10.1016/j.ijimpeng.2017.04.022>
- Madenci E, Oterkus S (2016) Ordinary state-based peridynamics for plastic deformation according to von mises yield criteria with isotropic hardening. *J Mech Phys Solids* 86:192–219. <https://doi.org/10.1016/j.jmps.2015.09.016>
- Bang DJ, Madenci E (2017) Peridynamic modeling of hyperelastic membrane deformation. *J Eng Mater Technol* 139(3):031007. <https://doi.org/10.1115/1.4035875>
- Roy P, Behera D, Madenci E (2020) Peridynamic simulation of finite elastic deformation and rupture in polymers. *Eng Fract Mech* 236:107226. <https://doi.org/10.1016/j.engfracmech.2020.107226>
- Rabczuk T, Ren H (2017) A peridynamics formulation for quasi-static fracture and contact in rock. *Eng Geol* 225:42–48. <https://doi.org/10.1016/j.enggeo.2017.05.001>

21. Zhang Y, Qiao P (2019) Peridynamic simulation of two-dimensional axisymmetric pull-out tests. *Int J Solids Struct* 168:41–57. <https://doi.org/10.1016/j.ijsolstr.2019.03.014>
22. Lu W, Oterkus S, Oterkus E (2020) Peridynamic modelling of hertzian indentation fracture. *Procedia Structural Integrity* 28:1559–1571. <https://doi.org/10.1016/j.prostr.2020.10.128>
23. Silling SA, Littlewood DJ, Seleson P (2015) Variable horizon in a peridynamic medium. *J Mech Mater Struct* 10:591–612. <https://doi.org/10.2140/jomms.2015.10.591>
24. Rahman R, Foster J (2016) Onto resolving spurious wave reflection problem with changing nonlocality among various length scales. *Commun Nonlinear Sci Numer Simul* 34:86–122. <https://doi.org/10.1016/j.cnsns.2015.10.003>
25. Ren H, Zhuang X, Cai Y, Rabczuk T (2016) Dual-horizon peridynamics. *Int J Numer Meth Eng* 108:1451–1476. <https://doi.org/10.1002/nme.5257>
26. Ren H, Zhuang X, Rabczuk T (2017) Dual-horizon peridynamics: A stable solution to varying horizons. *Comput Methods Appl Mech Eng* 318:762–782. <https://doi.org/10.1016/j.cma.2016.12.031>
27. Bobaru F, Yang M, Alves L, Xu SJJ (2009) Convergence adaptive refinement and scaling in 1d peridynamics. *Int J Numer Meth Eng* 77:852–877. <https://doi.org/10.1002/nme.2439>
28. Bobaru F, Ha YD (2011) Adaptive refinement and multiscale modeling in 2d peridynamics. *Int J Multiscale Comput Eng* 9:635–660. <https://doi.org/10.1615/IntJMultCompEng.20110.02793>
29. Dipasquale D, Zaccariotto M, Galvanetto U (2014) Crack propagation with adaptive grid refinement in 2d peridynamics. *Int J Fract* 190:1–22. <https://doi.org/10.1007/s10704-014-9970-4>
30. Gu X, Zhang Q, Xia X (2017) Voronoi based peridynamics and cracking analysis with adaptive refinement. *Int J Numer Meth Eng* 112:2087–2109. <https://doi.org/10.1002/nme.5596>
31. Madenci E, Oterkus E (2014) *Peridynamic Theory and Its Applications*. Springer, Berlin
32. Tada H, Paris PC, Irwin GR (2000) *The Stress Analysis of Cracks Handbook*. ASME Press, New York City
33. Kilic B, Madenci E (2010) An adaptive dynamic relaxation method for quasi-static simulations using the peridynamic theory. *Theoret Appl Fract Mech* 53(3):194–204. <https://doi.org/10.1016/j.tafmec.2010.08.001>
34. Wang B, Oterkus S, Oterkus E (2020) Derivation of dual-horizon state-based peridynamics formulation based on euler-lagrange equation. *Continn Mech Thermodyn*. <https://doi.org/10.1007/s00161-020-00915-y>
35. Sharon E, Gross SP, Fineberg J (1995) Local crack branching as a mechanism for instability in dynamic fracture. *Phys Rev Lett* 74(25):5096. <https://doi.org/10.1103/PhysRevLett.74.5096>
36. Fliiss S, Bhat HS, Dmowska R, Rice JR (2005) Fault branching and rupture directivity. *J Geophys Res Solid Earth*. <https://doi.org/10.1029/2004JB003368>
37. Belytschko T, Chen H, Xu J, Zi G (2003) Dynamic crack propagation based on loss of hyperbolicity and a new discontinuous enrichment. *Int J Numer Meth Eng* 58:1873–1905. <https://doi.org/10.1002/nme.941>
38. Borden MJ, Verhoosel CV, Scott MA, Hughes T, Landis CM (2012) A phase-field description of dynamic brittle fracture. *Computer Methods in Applied Mechanics & Engineering* 217–220(Apr.1):77–95. <https://doi.org/10.1016/j.cma.2012.01.008>
39. Kakouris EG, Triantafyllou SP (2019) Phase-field material point method for dynamic brittle fracture with isotropic and anisotropic surface energy. *Comput Methods Appl Mech Eng* 357:112503. <https://doi.org/10.1016/j.cma.2019.06.014>
40. Xu XP, Needleman A (1994) Numerical simulations of fast crack growth in brittle solids. *J Mech Phys Solids* 42(9):1397–1434. [https://doi.org/10.1016/0022-5096\(94\)90003-5](https://doi.org/10.1016/0022-5096(94)90003-5)
41. Kalthoff J (2000) Modes of dynamic shear failure in solids. *Int J Fract* 101:1–31. <https://doi.org/10.1023/A:1007647800529>
42. Kalthoff JF, Winkler S (1987) Failure mode transition at high rates of shear loading. In: Chiem CY, Kunze HD, Meyer LW (eds) *Impact Loading and Dynamic Behavior of Materials*, vol 1. pp 185–195
43. Zhang Z, Qiu Y, Hu Z, Ye H, Zhang H, Zheng Y (2022) Explicit phase-field total lagrangian material point method for the dynamic fracture of hyperelastic materials. *Comput Methods Appl Mech Eng* 398:115234. <https://doi.org/10.1016/j.cma.2022.115234>

Publisher's Note Springer Nature remains neutral with regard to jurisdictional claims in published maps and institutional affiliations.

Springer Nature or its licensor (e.g. a society or other partner) holds exclusive rights to this article under a publishing agreement with the author(s) or other rightsholder(s); author self-archiving of the accepted manuscript version of this article is solely governed by the terms of such publishing agreement and applicable law.